OVERVIEW OF MONO-ENERGETIC GAMMA-RAY SOURCES & APPLICATIONS*

F.V. Hartemann, F. Albert, G.G. Anderson, S. G. Anderson, A.J. Bayramian, S.M. Betts, T.S. Chu, R.R. Cross, C.A. Ebbers, S.E. Fisher, D. J. Gibson, A.S. Ladran, R.A. Marsh, M. J. Messerly, K.L. O'Neill, V. A. Semenov, M.Y. Shverdin, C.W. Siders, D.P. McNabb, and C.P.J. Barty, LLNL, Livermore, CA 94550, U.S.A.
A.E. Vlieks, E.N. Jongewaard, S.G. Tantawi and T.O. Raubenheimer, SLAC National Accelerator Laboratory, Stanford, CA 94025, U.S.A.

Abstract

Recent progress in accelerator physics and laser technology have enabled the development of a new class of tunable gamma-ray light sources based on Compton scattering between a high-brightness, relativistic electron beam and a high intensity laser pulse produced via chirped-pulse amplification (CPA). A precision, tunable Mono-Energetic Gamma-ray (MEGa-ray) source driven by a compact, high-gradient X-band linac is currently under development and construction at LLNL. High-brightness, relativistic electron bunches produced by an X-band linac designed in collaboration with SLAC NAL will interact with a Joule-class, 10 ps, diode-pumped CPA laser pulse to generate tunable γ-rays in the 0.5-2.5 MeV photon energy range via Compton scattering. This MEGa-ray source will be used to excite nuclear resonance fluorescence in various isotopes. Applications include homeland security, stockpile science and surveillance, nuclear fuel assay, and waste imaging and assay. The source design, key parameters, and current status are presented, along with important applications, including nuclear resonance fluorescence.

INTRODUCTION AND MOTIVATION

Recent work has been performed at LLNL to demonstrate isotope-specific detection of shielded materials via nuclear resonance fluorescence (NRF) using a tunable, quasi-monochromatic Compton scattering gamma-ray source operating between 0.2 MeV and 0.9 MeV photon energy. This technique is called Fluorescence Imaging in the Nuclear Domain with Energetic Radiation (or FINDER). This work has, among other things, demonstrated the detection of ^{7}Li shielded by Pb, utilizing gamma rays generated by a linac-driven, laser-based Compton scattering gamma-ray source developed at LLNL [1].

This program has also helped lay the theory and modeling foundations for isotopic imaging using NRF by benchmarking a complete suite of modeling codes against experiments, that can now be extended to address spatially-resolved, isotopic detection. The ability to produce isotope-specific images of unknown objects with deeply penetrating radiation will transform the special nuclear material (SNM) detection problem from simply identifying high optical depth cargo or high-Z materials to the unambiguous detection and verification of specific, dangerous contraband materials. The high spectral brightness and concurrent narrow bandwidth of this technology significantly reduces the radiological dose required for detection and largely eliminates artifacts due to small-angle elastic Compton scattering in the objects under interrogation. The highly-collimated, mono-energetic nature of the source also leads to simple detection protocols which can not only verify the presence of SNMs, but can also ascertain the absence thereof with a 99.9999% confidence level over a short interrogation time. Essentially, the phase space density of the gamma-ray beam used for interrogation or imaging is so high that discrimination against parasitic processes and backgrounds becomes both relatively simple to implement and highly effective [2].

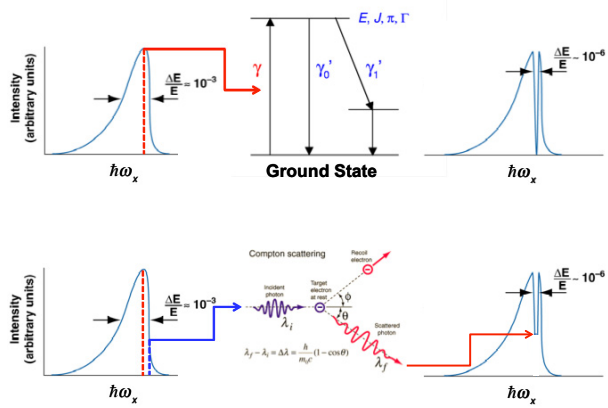

Fig. 1 Top: NRF. Bottom: parasitic process (Compton scattering) leading to potential notch refilling.

The two key components of this powerful detection scheme are the Compton scattering gamma-ray source and the detection unit; more specialized aspects of the system range from fiber laser-driven electron photo-injectors; high-brightness, high-gradient electron linacs; and hyper-dispersion chirped-pulse amplification (CPA) lasers; to sub-picosecond laser-electron synchronization techniques; advanced γ-ray modeling; and highly sensitive detectors.

The Laboratory is currently building a tunable, narrow-bandwidth, 3rd generation MEGa-ray source based on new high-gradient (> 65 MeV/m) X-band (11.424 GHz) rf accelerator structures capable of operating at 120 Hz, developed at SLAC NAL and built in collaboration with SLAC NAL; and laser technology developed for the previous T-REX (Thomson-Radiated Extreme X-Ray)

*This work is performed under the auspices of the U.S. DoE by LLNL under Contract DE-AC52-07NA27344 and supported by DNDO CFP06-TA-02-LL12.

source: a fiber-based photo-gun drive laser using frequency quadrupling and hyper-Michelson pulse shaping; and a 1 J, 10 ps, 120 Hz system using power amplification in diode-pumped Nd:YAG, operating near the Fourier transform limit with good beam quality, and utilizing proprietary LLNL hyper-dispersion stretching and compression technology. The compact accelerator also includes a custom, integrated focusing and transport lattice and interaction region designed to effectively shield parasitic x-ray production due to dark current. The facility is expected to produce γ-ray beams at a repetition rate of 120 Hz, with a peak brightness exceeding 10^{20} photons/(s x mm^2 x mrad^2 x 0.1% bandwidth).

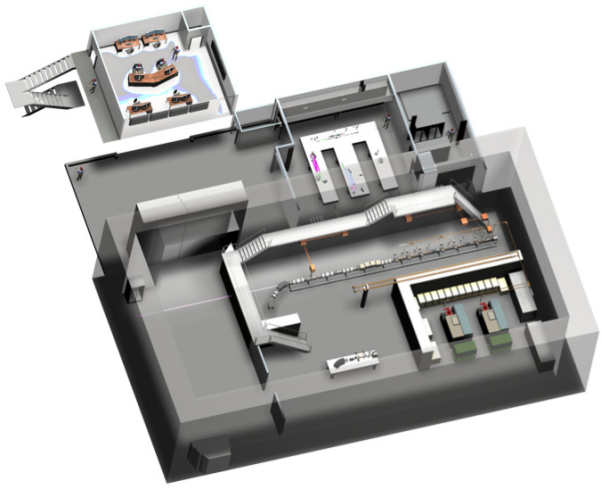

Fig. 2 LLNL proposed Compton scattering MEGa-ray facility.

COMPTON SCATTERING

This section is intended as a brief summary of the main properties of Compton scattering. The incident electron and photon 4-momenta are given by u_μ and k_μ; the scattered photon 4-wavenumber is q_μ, and the electron 4-velocity after the interaction satisfies energy-momentum conservation: $v_\mu = u_\mu + \hbar\left(k_\mu - q_\mu\right)$.

From these parameters, the incident and scattered light-cone variables can be computed: $\kappa = u_\mu k^\mu$, $\lambda = u_\mu q^\mu$ [3]. In QED units, the Compton formula is:

$$\kappa - \lambda = \hbar k_\mu q^\mu . \tag{1}$$

Note that the term on the right-hand side corresponds to recoil; it is absent in formalisms based on Thomson scattering. However, a simple ansatz allows for the inclusion of a recoil term in the radiation formula,

$$\frac{d^2N}{dqd\Omega} = \frac{\alpha}{4\pi^2} q \left| \int_{-\infty}^{\infty} \pi_\mu u^\mu \left(\tau\right) e^{-iq_\nu x^\nu(\tau)} \, d\tau \right|^2 . \tag{2}$$

Here, π_μ corresponds to the scattered 4-polarizations. In the case of a plane wave, the electron 4-velocity is described exactly by:

$$u_\mu = u_\mu^0 + A_\mu - k_\mu \frac{A_\nu \left(A^\nu + 2u_0^\nu\right)}{2k_\nu u_0^\nu} + \hbar k_\mu ; \tag{3}$$

where the last term will be shown to yield the appropriate recoil. Including the linear component of the 4-velocity in the radiation formula, and using the ballistic and recoil components, we find that:

$$\frac{d^2N}{dqd\Omega} = \frac{\alpha}{4\pi^2} q \left| \int_{-\infty}^{\infty} \pi_\mu \left(A^\mu - k^\mu \frac{A_\nu u_0^\nu}{k_\nu u_0^\nu} \right) e^{-iq_\nu \left[x_0^\nu + \left(u_0^\nu + \hbar k^\nu\right)\tau \right]} d\tau \right|^2 . \tag{4}$$

Replacing the 4-potential of the plane wave by $\varepsilon_\mu A_0 e^{ik_\nu x^\nu}$, where the incident 4-polarization is defined as

$$\varepsilon_\mu = \frac{1}{\sqrt{-A_\nu A^\nu}} \left(A_\mu - k_\mu \frac{A_\nu u_0^\nu}{k_\nu u_0^\nu} \right), \tag{5}$$

we find that the radiation integral reduces to:

$$\frac{d^2N}{dqd\Omega} = \frac{\alpha}{4\pi^2} \frac{q}{\kappa^2} A_0^2 \left| e^{-iq_\nu x_0^\nu} \right|^2 \left| \pi_\mu \varepsilon^\mu \right|^2 \left| \int_{-\infty}^{+\infty} e^{i\phi\left(1 - \frac{\lambda + \hbar q_\nu k^\nu}{\kappa}\right)} d\phi \right|^2 . \tag{6}$$

Eq. (6) clearly exhibits the coherence factor, the dipole scattering cross-section, and the Fourier transform of a delta-function containing the Compton formula; note that the electron phase in the incident plane wave, $\phi = k_\mu x^\mu$, has been used as the independent variable.

By comparison, the spin-independent component of the Lorentz-boosted Klein-Nishina differential cross-section [4] is:

$$\frac{d\sigma}{d\Omega} = \frac{\alpha^2}{2} \left(\frac{q}{\kappa}\right)^2 \left\{ \begin{array}{l} \frac{1}{2}\left(\frac{\kappa}{\lambda} + \frac{\lambda}{\kappa} - 2\right) + \\ 2\left[\varepsilon_\mu \pi^\mu - \frac{\left(\varepsilon_\mu u^\mu\right)\left(\pi_\mu v^\mu\right)}{\kappa} + \frac{\left(\varepsilon_\mu v^\mu\right)\left(\pi_\mu u^\mu\right)}{\lambda} \right]^2 \end{array} \right\} . \tag{7}$$

Taking the classical limit, where $\hbar = \hbar / m_0 c \to 0$, one sees that the Compton formula reduces to $\kappa = \lambda$, which also implies that $v_\mu = u_\mu$. It is then easily shown that the cross-section reduces to the Thomson dipole, $\left|\varepsilon_\mu \pi^\mu\right|^2$.

These quantities can then be used in conjunction with the phase space densities of the incident electrons and photons [5] to derive the spectral brightness of the source for a given scattering solid angle [6]. Typically, head-on collisions are considered because they yield the maximum relativistic Doppler upshift and minimal sensitivity to timing and synchronization; in such situations, one obtains spectra that are accurately described by the product of a Gaussian and an error function (for Gaussian phase space distributions). Using the full electron beam phase space as an input to the simulations yields more detailed spectra, as illustrated in Fig. 3. In general, the asymmetric low energy contribution on-axis can be traced back to the electron beam emittance, which results in a distribution of crossing angles at focus: some electrons do not contribute their maximum Doppler upshift in the direction of observation.

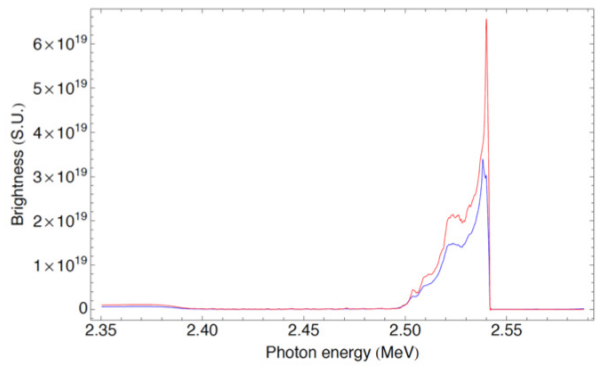

Fig. 3 Typical on-axis spectral brightness (see Table 1). The red curve corresponds to the linear brightness, and the blue curve includes weakly nonlinear ponderomotive effects.

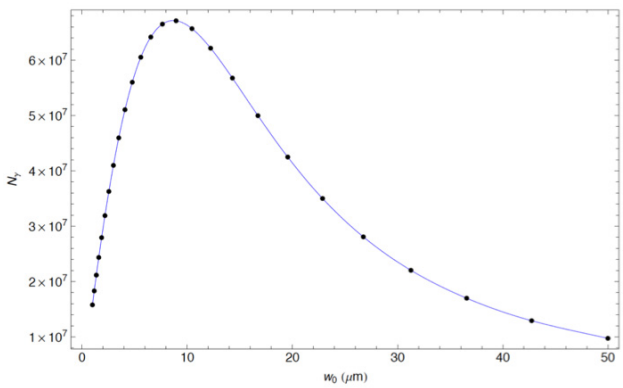

Fig. 4 Dose as a function of electron beam radius.

In Fig. 4, the electron beam focal spot size is varied, while the laser parameters are fixed, in order to determine how the total dose decreases when the beams are not properly matched. In conjunction with this optimization process, one must keep in mind the fact that, as the electron beam focusing increases, so does the γ-ray beam divergence.

From a technology viewpoint, the machine being built will use X-band (11.424 GHz) rf power produced by two SLAC NAL XL4 klystrons to energize a 5.59-cell rf gun with a Cu photocathode operating under gradients as high as 200 MV/m, and six SLAC NAL T53 sections running at 70 MeV/m accelerating gradient to produce a 250 pC electron beam at energies up to 250 MeV. The linac and gun brightness have been carefully optimized to deliver electron bunches at 120 Hz, with a normalized emittance of 0.4 mm.mrad; in particular, the rf fields have been symmetrized up to the quadrupole moment, and magnet tolerances have been specified to meet the system requirements. The HV modulators used to energize the XL4 klystrons are based on solid-state technology, with IGBT switches at the core of the system, driving a transformer with a very high secondary/primary voltage ratio.

The lasers used to produce the photo-electron bunches and the gamma-rays use a common fiber oscillator, which produces a train of light pulses at a precise sub-harmonic of the high-power rf. Pulses are selected out of the 40.8 MHz cw train to match the overall 120 Hz system repetition rate; these are stretched using hyper-CPA, amplified up to the mJ level with rare earth-doped fibers, further amplified in diode-pumped bulk heads to the J level for the interaction laser; finally the pulses are recompressed and frequency-multiplied.

Table 1: Source Parameters

Parameter	Linac	Laser
Energy/Wavelength	250 MeV	532 nm
Charge/Energy	0.25 nC	0.15 J
Duration	3 ps	8 ps
Focal spot	10 μm	10 μm
$\Delta\gamma/\gamma$/Bandwidth	0.1%	0.05 nm
Emittance/*f*-#	0.4 mm.mrad	20/50
Repetition rate	120 Hz	120 Hz

In conclusion, we have optimized the design of a high brightness Compton scattering gamma-ray source, specifically designed for NRF applications. Two different parameters sets have been considered: one where the number of photons scattered in a single shot reaches approximately 7.5 x 10^8, with a focal spot size around 8 μm; in the second set, the spectral brightness is optimized by using a 20 μm spot size, with 0.2% relative bandwidth.

REFERENCES

[1] F. Albert *et al*., Opt. Lett. 35, 354 (2010).
[2] J. Pruet *et al*., J. Appl. Phys. 99, 123102 (2006).
[3] L.M. Brown & R.P. Feynman, Phys. Rev. 85, 231 (1952).
[4] G. Bhatt *et al*., Phys. Rev. A28, 2195 (1983).
[5] E. Wigner, Phys. Rev. 40, 749 (1932).
[6] F.V. Hartemann *et al*. Phys. Rev. STAB 8, 100702 (2005).